CrossMark

RESEARCH PAPER

Hydrodynamic focusing for microfluidic impedance cytometry: a system integration study

Thomas E. Winkler[1,2] · Hadar Ben-Yoav[3] · Reza Ghodssi[1,2]

Abstract We present the first in-depth system integration study of in-plane hydrodynamic focusing in a microfluidic impedance cytometry lab-on-a-chip. The method relies on constricting the detection volume with non-conductive sheath flows and characterizing particles or cells based on changes in impedance. This approach represents an avenue of overcoming current limitations in sensitivity with translating cytometers to the point of care for rapid, low-cost blood analysis. While examples of integrated devices are present in the literature, no systematic study of the interplay between hydrodynamics and electrodynamics has been carried out as of yet. We develop analytical and numerical models to describe the impedimetric response of the sensor as a function of cellular characteristics, physical flow properties, and device geometry. We fabricate a working prototype lab-on-a-chip for experimental validation using latex particles. We find that ionic diffusion can be a critical limiting factor even at high Péclet number. Moreover, we explore geometric variations, revealing that the ionic diffusion-related distance between the center of the hydrodynamic focusing junction and the impedance measurement electrodes plays a dominant role. With our device, we demonstrate over fivefold enhancement in impedance signals and population separation with in-plane hydrodynamic focusing. It is only through such in-depth system studies, in both models and experiments, that optimal utilization of microsystem capabilities becomes possible.

Keywords Microsystem integration · Microfluidics · Impedance cytometry · Hydrodynamic focusing · Diffusion

✉ Reza Ghodssi
   ghodssi@umd.edu

1   MEMS Sensors and Actuators Laboratory (MSAL), Institute for Systems Research, Department of Electrical and Computer Engineering, University of Maryland, College Park, MD 20742, USA

2   Fischell Department of Bioengineering, University of Maryland, College Park, MD 20742, USA

3   Department of Biomedical Engineering, Ben-Gurion University of the Negev, 8410501 Beer Sheva, Israel

List of symbols

Symbol	Description
$\varnothing$ (µm)	Cell diameter
VA (µm)	Virtual aperture width
Q_s, Q_f (µl/h)	Flow rates of sample and focus streams
FR (1)	Flow ratio (sample flow over total flow)
Z, Z_{empty} (Ω)	Impedance, empty channel impedance
$|\Delta Z|$ (%)	Relative change in impedance (impedance signal)
$\Delta|\Delta Z|$ (%)	Population separation
δ (%)	Population spread
w, w_{fc} (µm)	Center (sample) and focus channel width
h (µm)	Channel height
l, g (µm)	Microelectrode length and gap
d (µm)	Distance from focus junction to electrode

med, el, DI, ion, cell, mem, cyt	Subscripts denoting: medium, electrolyte component of medium, DI water component of medium, ions in the medium, cells in the medium, membrane component of cell, cytosol component of cell
P, V (μm^3)	Particle and electrical interaction volume
Π (1)	Volume fraction of particle in electrical interaction volume
σ (S/m)	Conductivity
ε (F/m)	Permittivity
C (1)	Normalized concentration
IS (M)	Ionic strength
λ_D (μm)	Debye length
C_{offset}, C_{amp} (1)	Concentration profile fit parameters
s_p, s_s (μm)	Concentration profile fit parameters
f, f_s (Hz)	Signal and sampling frequency
Pe, Re (1)	Péclet number, Reynolds number
RMSE (%)	Root-mean-square error

1 Introduction

For a wide range of applications, from medicine to environmental monitoring to materials science, the characterization of large populations of individual particles is of great interest. This is especially true for the analysis of cells, where blood cell counts have been a core diagnostic marker for over a century (Kottke-Marchant and Davis 2012). The utility of cell studies increases significantly when not only interrogating counts, but also size, surface markers, interior composition, etc. (Shapiro 2003). The laboratory gold standard is flow cytometry, where thousands of cells are rapidly analyzed within a matter of seconds. This technology enables one of the most commonly performed diagnostic tests, the blood differential, which categorizes all blood cell types. Today, applications also extend far beyond, from stem cell research to circulating tumor cell analysis. In the generally bulky flow cytometers, a blood sample is focused to flow its cells past various detectors single-file. Typical methods include laser light scattering and absorption, fluorescent labels for population-specific surface antigens (*e.g.,* CD4, CD8…), or impedance measurements. However, the reliance on labels and complex optics represents a major barrier to translating this technology to the point of care (Bashir 2004; Jung et al. 2015). There, it would significantly benefit both patients and physicians through immediate results, decreased costs, and increased accessibility, especially in remote locations.

The impedance measurement aspect is ideally suited for translation into small, portable lab-on-a-chip (LOC)-type devices (Ateya et al. 2008; Cheung et al. 2010; Sun and Morgan 2010; Chen et al. 2015; Mansor and Ahmad 2015). Miniaturization of electronics is much more advanced than for optics, and a commercial integrated circuit impedance analyzer is available for less than $10 (Analog Devices 2005). Impedance cytometry is an extension of the Coulter principle, where a particle or cell of diameter ⌀ passing through an aperture of diameter A changes the measured impedance Z across that aperture by $|\Delta Z| \propto \varnothing^3/A^2$ (relative to the empty aperture impedance Z_{empty}) (DeBlois and Bean 1970). Alternating current (AC) interrogates the more generalized changes in dielectric properties within the interaction volume and thus more cellular information than just size (Gawad et al. 2001, 2004). Recently, multi-frequency impedance cytometry has been presented as a promising method to perform the critical task of differential blood analysis with LOCs (Holmes et al. 2009; van Berkel et al. 2011; Han et al. 2012; Nguyen et al. 2015; Frankowski et al. 2015). However, current implementations still suffer from limited resolution, with differentiation of some white blood cell types such as monocytes and granulocytes relying on the addition of chemical reagents to the sample, and no categorization of granulocyte sub-types demonstrated.

In this paper, we study integration of in-plane hydrodynamic focusing with impedance cytometry in an LOC, an approach that may enable overcoming previous limitations in sensitivity. Hydrodynamic focusing relies on laminar flow in microfluidics, wherein a sample flow Q_s is constricted (or focused) by introducing additional sheath flows Q_f. A theoretical description of the phenomenon has recently been derived (Lee et al. 2006). For impedance cytometry, its potential utility becomes apparent when considering non-conductive sheath fluids. This decreases the effective electrical interaction volume by providing a virtual aperture (VA). In the aforementioned simplified analysis of the impedance signal $|\Delta Z|$, this is equivalent to a decrease in A, which directly translates to an increase in sensitivity in terms of cell size and properties. Moreover, in contrast to physical channel confinement, this is inherently more versatile—it can be freely adjusted through Q_f, to the first order independent of device geometry and throughput Q_s. Additionally, a virtual rather than physical aperture limits the danger of clogging.

A few studies have previously demonstrated the advantages of in-plane hydrodynamic focusing in impedance cytometry. Bernabini et al. (2011) and Evander et al. (2013) utilized oil sheaths to enable impedance analysis of very small particles, specifically bacteria and platelets. However, the interplay of focusing and sensitivity is only cursorily discussed in theory or experiments, respectively. Rodriguez-Trujillo et al. (2007) implemented deionized (DI)

water sheaths for particle counting. While their research considers hydrodynamic aspects in depth, it suffers from limited experimental data on cytometry performance. In parallel, a lot of research has been devoted to addressing a shortcoming of in-plane focusing, namely the lack of confinement in the out-of-plane direction (Ateya et al. 2008; Cheung et al. 2010; Sun and Morgan 2010). This can be accomplished, *e.g.,* by adding additional sheath flows, an approach that has been systematically studied in both models and experiments (Nieuwenhuis et al. 2004; Rodriguez-Trujillo et al. 2008; Watkins et al. 2009) or by relying on non-hydrodynamic forces ranging from acoustic to inertial (Xuan et al. 2010; Golden et al. 2012).

Yet, to date there remains a need for similar systematic study of the interplay of in-plane hydrodynamic focusing—the foundation of many more elaborate approaches—and impedance cytometry performance. Here, we present the first such study on systems integration. In Part A, we develop analytical and numerical models to understand the impact of hydrodynamic flow parameters on particle measurements. In Part B, we utilize an LOC platform—shown in Fig. 1—to experimentally demonstrate the interplay of

flow rates and sensitivity. For systems integration, investigating limitations from both the theoretical and experimental standpoints is of critical importance. We further explore the potential impact of geometric variations, which has rarely been considered in hydrodynamic focusing. Overall, our results highlight the potential of this approach in overcoming previous limitations of LOC impedance cytometers and yield important guidelines for future implementation.

2 Methods

2.1 Device design

We propose a simple design, shown in Fig. 1, comprising two physical layers. The first layer incorporates coplanar microelectrodes ($l = 25$ μm width, $g = 25$ μm gap) for impedance measurements. The microfluidic channels ($h = 20$ μm height) constitute the second layer. To investigate geometry variations, we combined focus channel widths $w_{fc} = 25$, 50 and 75 μm with constant center channel width $w = 50$ μm. We made extensive use of modeling
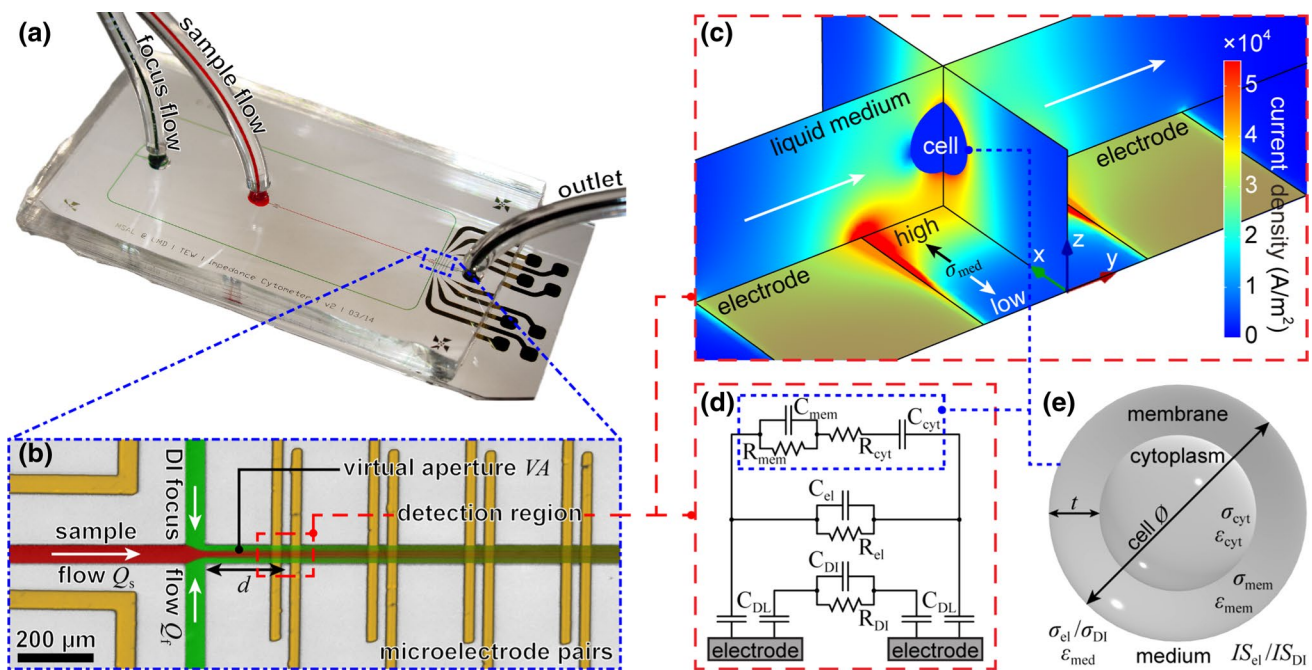

Fig. 1 a Photograph of our impedance cytometry LOC. The microfluidic channels are filled with dye to enhance visualization. **b** Micrograph of the region of interest highlighted by the *blue dash-dotted box* in **a**. In-plane hydrodynamic focusing is schematically illustrated by overlaid numerical simulation for a 1:1 ratio of sample (particles in electrolyte; *red*) to focus (DI water; *green*) flows. The virtual aperture (VA) sample confinement is conserved downstream, where impedance is measured across the first gold microelectrode pair, separated from the junction by distance *d*. **c** Numerical impedance cytometry model corresponding to the *red dashed box* in **b**. The cell (*center*) is sus-

pended in a microchannel between two electrodes (*bottom*; *gold rectangles*). The *colors* correspond to the current density from *blue* (*low*) to *red* (*high*), clearly illustrating the diffusely focused electrolyte, with conductivity σ_{med} ranging from high in the center to low on either side. **d** Analytical equivalent circuit model corresponding to the *red dashed box* in **b**. Shown for VA > ø, this accounts for conduction pathways from the cell (*top*), the electrolyte (*middle*), as well as the ionic double layer capacitance and the DI water aperture (*bottom*). **e** Model of a cell as a spherical shelled particle consisting of cytoplasm and membrane, surrounded by liquid medium (color figure online)

to guide the design process. Critical parameters were chosen based on model optimization combined with experimental and biological constraints.

2.2 Analytical hydrodynamic model

For an analytical description of in-plane hydrodynamic focusing, we apply the model derived by Lee et al. (2006) for the relevant case of a central sample stream (flow rate Q_s) met perpendicularly by two symmetric focus streams (combined flow rate Q_f):

$$\frac{Q_s}{Q_s + Q_f} = \frac{VA}{w} \gamma(VA, w, h) \tag{1}$$

Therein, the function γ is defined as in (Lee et al. 2006), with w the sample channel width, h the channel height, and VA the virtual aperture width effected by flow focusing.

2.3 Numerical hydrodynamic model

Our numerical models of hydrodynamic focusing were constructed in COMSOL Multiphysics (Burlington, MA) utilizing the Creeping Flow and the Transport of Diluted Species modules. A central sample flow of fast-diffusing ionic species [$D_{ion} = 1683$ μm²/s; average of dominant sodium and chloride ion diffusion coefficients (Lide and Kehaian 1994)] and slow-diffusing particles [$D_{cell} = 0.1$ μm²/s; red blood cell diffusion coefficient (Berg 1993)] is met by focus flows of DI water at a right angle. In the model solutions, we evaluated the concentration profiles $C(x)$ at a distance d downstream from the focusing junction. Specifically, $C(x)$ describes the cross-sectional average (along the height of the channel) concentration, normalized to the input concentration (*i.e.*, such that without flow focusing $C = 1$). For further analysis, this was fitted in OriginPro (OriginLab Corporation; Northampton, MA) using a symmetric double sigmoidal peak function:

$$C(x) = C_{offset} + \frac{1}{2} C_{amp} \left(\tanh \frac{2x + s_p}{4s_s} - \tanh \frac{2x - s_p}{4s_s} \right) \tag{2}$$

In Fig. 2, we show an example of such a normalized cross-sectional concentration profile (blue dots) and fit (orange line) across the width of the channel. Analytically, diffusion profiles can be described by the sigmoidal error function. The symmetric double sigmoidal above serves as an approximation that captured all investigated concentration profiles well, with maximum fitting root-mean-square errors at RMSE < 2 %. The parameters, illustrated with black dashed lines, denote the function's offset from zero (C_{offset}), the amplitude of the double sigmoidal peak (C_{amp}), its full width at half maximum (s_p), and the width of the sigmoidal slope (s_s; inversely proportional to the steepness
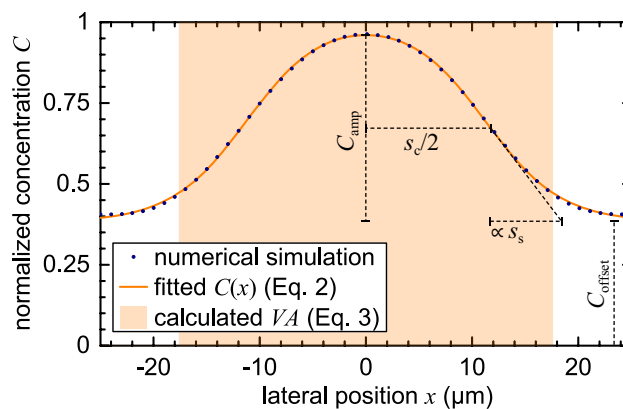

Fig. 2 Concentration (averaged along the height of the channel and normalized to the input concentration) as a function of lateral position in the channel for an exemplary FR = 0.75 (total flow 40 μl/h). The plot shows both numerical data (*blue dots*) as well as the corresponding fit with Eq. 2 (*orange line*). The fit parameters are illustrated with *black dashed lines*, and the corresponding VA according to Eq. 3 is overlaid as an *orange rectangle* (illustrating a discrete-phase concentration profile resulting in the same VA value) (color figure online)

of the slope). Although VA is not clearly defined, we approximate it from the four fit parameters as:

$$VA = C_{amp}(s_p + s_s) + \frac{C_{offset}}{C_{offset} + C_{amp}} w \tag{3}$$

The resulting VA for the example in Fig. 2 is illustrated as a discrete-phase concentration profile with equivalent VA (shaded rectangle). The first term captures the focused concentration profile and is roughly analogous to taking the integral over the double sigmoidal peak (without offset), then calculating the equivalent width of a discrete phase that would yield the same integral. The second term captures non-ideal focusing—the numerator accounts for the integral over the offset area under the double sigmoidal peak baseline; the denominator scales the importance of this "background" to the prominence of the peak. This form ensures that in the limiting case of no diffusion between sample and focusing flows (*i.e.*, discrete phases; $C_{offset} = 0$, $C_{amp} = 1$, $s_s = 0$), it reduces to $VA = s_p$. Conversely, for the case of complete mixing (*i.e.*, a flat concentration profile; $C_{amp} = 0$, $C(x) = C_{offset}$), it reduces to $VA = w$, reflecting the equivalence to a simple change in input concentration.

2.4 General cell model

For impedance cytometry purposes, cells can generally be modeled as spherical shelled particles (Fig. 1e) with a membrane (thickness $t = 5$ nm, conductivity $\sigma_{mem} = 10$ nS/m, permittivity $\varepsilon_{mem} = 11.3\ \varepsilon_0$) enveloping a cytoplasmic compartment ($\sigma_{cyt} = 0.6$ S/m, $\varepsilon_{cyt} = 60\ \varepsilon_0$), suspended in a liquid medium (σ_{med}, $\varepsilon_{med} = 78\ \varepsilon_0$) (Morgan et al. 2007). We note

that the spherical shelled particle approximation neglects a number of factors, such as cell shape and internal cell structure. While even analytical—not to mention numerical—refinements have been published, *e.g.,* for ellipsoids (Asami et al. 1980), experiments have shown acceptable agreement with spherical models for a wide range of blood cell types (Cheung et al. 2005; Holmes et al. 2009).

2.5 Analytical electrodynamic model

Our model integrates a number of separately published approaches from literature, which account for a complete equivalent circuit model of a spherical shelled particle via Maxwell's mixture theory (Sun et al. 2007a, 2010), the non-uniform electric field of co-planar electrodes (Sun et al. 2007b), and the interfacial ionic double layer (Morgan et al. 2007). We model the latter using a Helmholtz approximation of parallel plate capacitors at the electrodes, with capacitance $F = w\, l\, \varepsilon_{med}/\lambda_D(IS)$, where λ_D is the Debye length as a function of the respective ionic strength [$IS_{el} = 0.16$ M (Siggaard-Andersen et al. 1984), $IS_{DI} = 0.1$ μM]. To account for hydrodynamic focusing, we assume discrete phases of particle-suspending electrolyte [$\sigma_{el} = 1.6$ S/m (Johnson et al. 2005)] sample flow as well as DI water ($\sigma_{DI} = 5.5$ μS/m) sheath flow, the latter yielding a parallel conduction pathway. The resulting equivalent circuit model of capacitors C and resistors R for the case of VA > ∅, where the cell is fully enveloped in electrolyte, corresponds to Fig. 1d.

To further expand our model into the VA < ∅ regime, where the cell is partially exposed to DI water, we consider the volume fraction $\Pi = P/V$. Analogous to $∅^3/A^2$ in the earlier simplified analysis, it represents the most significant parameter affecting impedance signals $|\Delta Z|$. The volume fraction defines the ratio of the particle volume $P = 1/6\, \pi\, ∅^3$ to the electrical interaction volume $V_{el} = \kappa\, VA\, h\, (g + 2\, l)$. The cell constant of the cytometer κ is derived by using Schwarz-Christoffel mapping and serves to account for the non-homogenous electric field (Sun et al. 2007b). In the VA < ∅ regime, the particle partially resides in both the electrolyte and the water phase. Thus, we define two distinct particle volumes $P_{el} = 1/12\, \pi\, VA\, (3∅^2 - VA^2)$ and $P_{DI} = P - P_{el}$ [with corresponding $V_{DI} = \kappa\, (w - VA)\, h\, (g + 2l)$], respectively, capturing the volumes of the central spherical segment inside VA and the spherical caps outside.

2.6 Numerical electrodynamic model

The numerical electrodynamic model was constructed in COMSOL Multiphysics utilizing the Electric Currents and Electrical Circuit modules. The cell is modeled as a homogenous sphere with properties derived through Maxwell's mixture theory based off the aforementioned spherical shelled particle model (Sun et al. 2008). To describe the suspending liquid medium, the normalized variable ion concentration $C_{ion}(x)$ from hydrodynamic modeling is coupled in via Eq. 2. Specifically, a continuous liquid phase is approximated with laterally varying conductivity $\sigma_{med}(x) = \sigma_{el} \times C_{ion}(x)$. The ionic double layer is modeled as a series capacitance at the electrodes, with a Helmholtz approximation for the interfacial capacitances similarly modified to $F = \int_{electrode} \varepsilon_{med}/\lambda_D(IS_{DI} + IS_{el} \times C_{ion}(x))$. We note that our approach neglects the variation of molar conductivity with ion concentration (Pitts and Tabor 1970). However, such a description becomes exceedingly complex for multi-ionic electrolytes such as PBS or human serum, and the predicted error of our linear approximation for $\sigma_{med}(C_{ion})$ remains on the order of only 15 % even at high dilutions for such electrolytes (Johnson et al. 2005).

2.7 Model analysis

To compare models, we utilize the relative (unless otherwise noted, with respect to the numerical model) RMSE as calculated in OriginPro. The software was similarly used to perform partial least squares (PLS) analysis.

2.8 Device fabrication

The devices were fabricated following standard photolithography (Ben-Yoav et al. 2014) and soft lithography (Meyer et al. 2015) procedures. In brief, electrodes were wet-etched in gold/chrome (190 nm/20 nm) e-beam deposited on Borofloat 33 glass wafers (University Wafer, Boston, MA). Microfluidics were cast in poly(dimethylsiloxane) (PDMS; Sylgard 184; Dow Corning, Washington, DC) from a SU8-2015 (MicroChem, Westborough, MA) negative mold on a silicon wafer substrate (Ultrasil, Hayward, CA). After dicing, the separate layers were aligned and oxygen plasma-bonded to place the active electrode pair a distance $d = 170$ μm downstream from the hydrodynamic focusing junction, as shown in Fig. 1b. The other microelectrode pairs are not utilized in this study. All component dimensions were verified to be within 10 % of the design parameters using contact profilometry (Dektak 6 M; Veeco, Plainview, NY), optical profilometry (NT1100; Veeco), and optical microscopy.

2.9 Flow conditions

For our theoretical and experimental study, we choose a constant total flow rate of $Q_s + Q_f = 40$ μl/h. By adjusting the relative ratio between flow rates, flow ratios from FR = 0.875 down to 0.075 were explored. While the chosen flow rates are significantly slower than those in many application-driven microfluidic cytometers in the

literature (Cheung et al. 2010), our experimental conditions ensure creeping flow (Re < 1; *cf.* Online Resource 1) and allow us to more closely study systems interplay parameters. We note that the slower flow rate also reduces requirements concerning readout equipment, opening up the real possibility of integration with a low-cost commercial integrated circuit impedance analyzer (Analog Devices 2005).

2.10 Measurements

The LOC fluidic ports were connected to syringes (inlets) and a waste reservoir (outlet) utilizing Tygon tubing (0.19 mm ID, 2.03 mm OD; Cole-Parmer, Vernon Hills, IL). Sample and DI water flow was provided by NE-1002X syringe pumps (New Era Pump Systems, Farmingdale, NY). Prior to use, the LOCs were rinsed with human serum (Sigma-Aldrich, St. Louis, MO) to reduce PDMS hydrophobicity. For the sample stream, polystyrene particles ($\varnothing = 6$ and 10 μm; sulfate-type; Life Technologies, Carlsbad, CA) were suspended in phosphate-buffered saline (PBS; $1 \times$ from tablet) with 10.9 % (w/w) sucrose (Fisher Scientific, Waltham, MA). The added sucrose served to reduce the particle settling velocity through density matching. The LOC was connected to an E4980A Precision LCR Meter (Agilent, Santa Clara, CA) using spring-loaded pins and coaxial cables. Experiments were conducted at an applied AC potential $U = 1$ V with frequency $f = 100$ kHz, with a sampling frequency for Z of $f_s \sim 180$ Hz. Flow control and data recording was implemented through LabView (National Instruments, Austin, TX). Data were collected for 0.5–2 h depending on Q_s to ensure sufficient statistical sample size >1000 particles for each device and FR.

2.11 Experimental analysis

The background signal Z_{empty} was determined from the raw recorded Z using MATLAB (MathWorks, Natick, MA) by applying a temporal 9 Hz low-pass filter after eliminating obvious peaks and outliers (cut-off based on second derivative). Subsequently, $|\Delta Z|$ was calculated, peaks were detected using MATLAB's algorithms, and the data were transformed into histograms. Population averages and spreads were calculated using Gaussian histogram peak fits between the first and second minima in the distribution with OriginPro. To compare models and data fits, we utilize the relative (unless otherwise noted, with respect to the model) RMSE. The software was similarly utilized to perform analysis of variance (ANOVA), reported in terms of p values.

3 Results and discussion

3.1 Part A: theory

The purpose of our models is to predict the impact of external control parameters on impedance cytometry performance. This is characterized as the relative change in impedance $|\Delta Z| = (Z_{particle} - Z_{empty})/Z_{empty}$ caused by a cell or particle passing through the detector and as the separation between different cell populations i and j, $\Delta|\Delta Z| = |\Delta Z|_i - |\Delta Z|_j$. Intuitively, the main parameters of interest are the flow rates Q_s and Q_f, but the models can also be utilized to reveal other dependencies, such as geometrical ones. These theoretical models of systems interplay are essential for both guiding device design and elucidating the physical underpinnings of experimental observations. To the best of our knowledge, we present the first such models and analysis.

3.1.1 Hydrodynamic models

As previously discussed, the virtual aperture (VA) provided by non-conductive sheath flows to confine the sample flow is expected to be the critical parameter affecting impedance cytometry with in-plane hydrodynamic focusing. Control of VA, however, is not direct but relies on control of the respective flow rates Q_s and Q_f. This hydrodynamic problem has previously been studied in theory and experiments (Lee et al. 2006; Watkins et al. 2009; Nasir et al. 2011; Kunstmann-Olsen et al. 2012). However, before proceeding to analyze the coupled hydrodynamic/electrodynamic system, we still need to consider this aspect separately. Critically, we need to consider the difference in prediction of VA between analytical and numerical models—comparing this effect size to that observed in the impedance cytometry models will allow us to isolate purely hydrodynamic or electrodynamic effects from those arising through systems interactions.

The aforementioned previous studies of in-plane hydrodynamic focusing include an analytical description, given here in Eq. 1 (Lee et al. 2006). It reveals that the flow ratio of sample to total flow FR $= Q_s/(Q_s + Q_f)$ is the main determining factor for VA—and thus, intuitively, impedance cytometry sensitivity—for a given channel geometry, and assuming laminar flow. At the same time, we note that the throughput, equal to Q_s, remains decoupled.

In contrast to the analytical model, our numerical model, overlaid in Fig. 1b, accounts for diffusion both for ions—which determine conductivity and thus ultimately define VA—as well as for the cells themselves. Moreover, the numerical approach allows for variation of geometrical parameters that the analytical model does not consider,

such as the focus channel geometry (*e.g.,* focus inlet width w_{fc}). With diffusion eliminating the discrete nature of the liquid phases, however, VA is not clearly defined. Instead, we approximate VA based on a parametric description of the cross-sectional ion concentration profiles in the detection region (Eq. 3).

We plot the predicted virtual aperture width VA for a range of flow ratios FR from both analytical (dotted line) and numerical (crosses) modeling at the subsequently used experimental conditions in Fig. 3a. Cellular confinement from numerical modeling is also indicated (circles). As intuitively expected, a lower FR effects a narrower VA, with the higher contribution of the focusing flows confining the sample flow more and more. The plot also shows noticeable deviation between the analytical and numerical predictions for ions, with the latter consistently predicting a wider VA. As expected, the cells match the analytical model more closely due to the decreased importance of diffusion. Statistical analysis quantifies the deviation from the

(a)

(b)   **(c)**

Fig. 3 Hydrodynamic analytical (*dotted line*) and numerical (*orange crosses*) models revealing the dependence of the virtual aperture width VA on: **a** the flow ratio FR in the experimental regime (constant total flow), with numerical results for slow-diffusing cells (*red circles*) also presented for comparison; **b** the sample flow rate Q_s for a representative, fixed FR = 0.25; **c** the focus channel width w_{fc} for a representative, fixed FR = 0.25 (color figure online)

analytical prediction as RMSE = 17.6 % (ions) and 8.9 % (cells). The speculative nature of Eq. 3 likely contributes to especially the underestimation of VA for cells, where better agreement might be expected between the models. Still, the magnitude of the deviation between cells and ions is less sensitive in this regard and can serve as a first-order approximation, as evidenced also later in considering the empty channel impedance. Thus, we might expect ionic diffusion to ultimately show similar, appreciable yet limited effect size in impedance cytometry performance.

To further consider the impact of diffusion, we look at the impact of the sample flow rate Q_s on VA for a representative flow ratio FR = 0.25 in Fig. 3b (the full interdependency is explored in Online Resource 1). As the flow rate increases, the time for diffusion of ions from the sample stream into the focus streams decreases, leading to a more well-defined virtual aperture. Indeed, the numerical model prediction (crosses) rapidly falls from the upper limit of VA = 50 μm—corresponding to complete interdiffusion across the channel width w—toward the lower limit of the analytical model (dotted line). The experimental $Q_s = 10$ μl/h falls in the asymptotic approach to the latter, with large additional increases only yielding minor changes in VA.

In Fig. 3c, we also explore the impact of geometrical variations—specifically in the width of the focus channel w_{fc}—on VA at a representative FR = 0.25. The numerical model reveals a positive correlation between the parameters. However, from the almost two order-of-magnitude difference in *y*-axes scales between this plot and Fig. 3a, b, these variations appear insignificant compared to those achievable through the flow ratio FR. Indeed, the variation with w_{fc} of RMSE = 1.4 % around the mean is well below the expected inherent experimental variability in FR due to syringe pump stepping. The negligible impact of the focus channel width w_{fc} on VA predicted here is in contrast to the few other studies on in-plane hydrodynamic focusing geometry, which considered confluence angle (Nasir et al. 2011; Kunstmann-Olsen et al. 2012). This angle was demonstrated to have significant impact, with VA widening by up to 50 % at an angle of 10° versus 90°. The result that 90° proved optimal for flow focusing over sub-millimeter distances also motivated our choice of this geometry for the work presented here.

3.1.2 Electrodynamic models

On top of the description of hydrodynamics, we require a relation of the virtual aperture width VA, as well as various geometrical parameters, to the impedance cytometry performance. The analytical electrodynamic model for that purpose, further detailed in the Methods, reduces the relevant components of the impedance cytometer and the cell
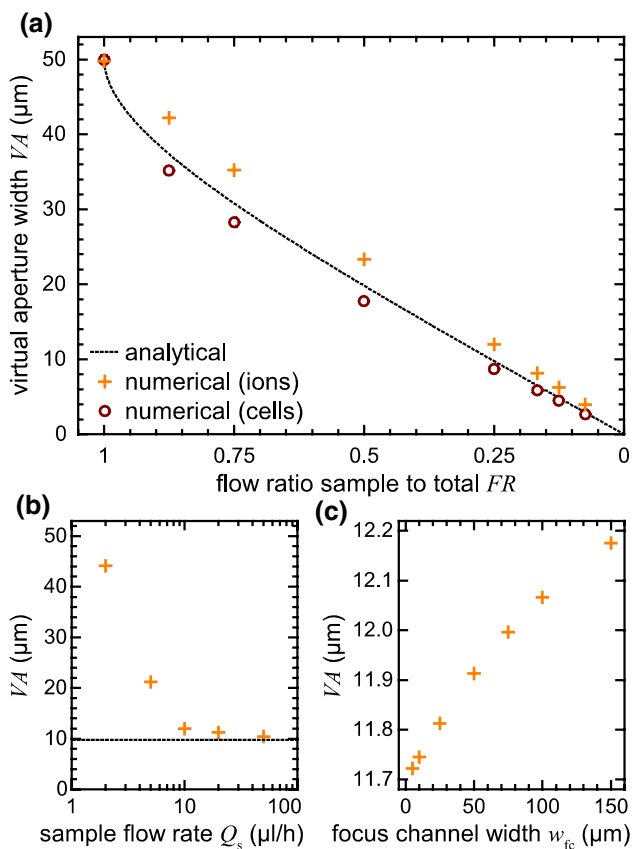
into an equivalent circuit model of capacitors C and resistors R (Fig. 1d) between the electrodes. Combining the hydrodynamic and electrodynamic models, we obtain the first comprehensive analytical model for impedance cytometry with in-plane hydrodynamic focusing, available as Online Resource 2. It predicts impedance signals $|\Delta Z|$ as a function of flow rates, sample channel geometry, electrode geometry, cell properties, etc.

To numerically model impedance cytometry, we set up 3D simulations as shown in Fig. 1c. The model applies an AC potential across the electrodes inside a microfluidic channel section with a cell centrally suspended in liquid. Coupling in the cross-sectional ion concentration profile from hydrodynamic modeling (corresponding to VA; *cf.* Methods) for a continuous description of the electrolyte yields a comprehensive numerical model. The biggest advantage over the analytical model is that it accounts for diffusion effects, but it can also be applied to explore analytically inaccessible parameters like cell positioning.

For subsequent considerations—both theoretical and experimental—in our comprehensive impedance cytometry study, we will focus on a solely cell size-sensitive frequency of 100 kHz. In this frequency regime, cells (or other complex core/shell particles) interact with the electric field as insulating spheres, as illustrated in Online Resource 1. This allows us to treat cells and polystyrene particles equivalently, simplifying experimental procedures while not compromising the general nature of our models. The chosen diameters of $\varnothing = 6$ and 10 μm correspond roughly to red (Cheung et al. 2005) and white (Holmes et al. 2009) blood cell sizes, respectively.

In Fig. 4a, b, we evaluate the potential benefits of integrating in-plane hydrodynamic focusing with impedance cytometry. We plot the relative impedance signal $|\Delta Z|$ for cells of diameter $\varnothing = 6$ μm (a), as well as the separation between the $\varnothing = 6$ and 10 μm cell diameter populations

$\Delta|\Delta Z|$ (b), as a function of flow ratio FR from both the analytical (dotted lines) and the numerical (squares, crosses) models. The enhancement in impedance cytometry performance becomes immediately apparent from the increase in both $|\Delta Z|$ and $\Delta|\Delta Z|$ with decreasing FR for both models. These trends are also conserved for membrane and cytoplasm properties at higher frequencies (not shown). The results fit with the initial hypothesis of enhanced impedance cytometry performance with hydrodynamic focusing.

Comparing numerical and analytical models, we find similar trends from flow ratio FR = 1 down to 0.5, but large deviation toward lower values. In the analytical models, toward very low FR, the signals saturate only once VA < $\varnothing$, where a further narrowing of VA decreases not only the denominator (electrical interaction volume V_{el}) but also the numerator (effective particle volume P_{el}) in the volume fraction Π. In the numerical model, however, saturation sets in much earlier and significantly hampers the enhancement in both $|\Delta Z|$ and $\Delta|\Delta Z|$—down to 2.8-fold from up to tenfold in the analytical model. Expressing the deviation in $\Delta|\Delta Z|$ between numerical and analytical models quantitatively in terms of RMSE, we obtain 41 versus 203 % in the high (1–0.5) and low (0.5–0) FR regimes, respectively. We attribute this to diffusion effects, the main difference between the models. Overall, while we expect similar behavior in experiments, we acknowledge that all our models neglect more complex hydrodynamic effects. This includes variations along the height of the channel as well as the boundary layer that would form around the cell or particle, which would likely impact the particulars of these trends.

To again consider diffusion effects further, we plot the population separation $\Delta|\Delta Z|$ as a function of sample flow rate Q_s at a representative, fixed FR = 0.25 in Fig. 4c. We see that the numerical model data (crosses) rises only gradually toward the upper limit of the analytical solution
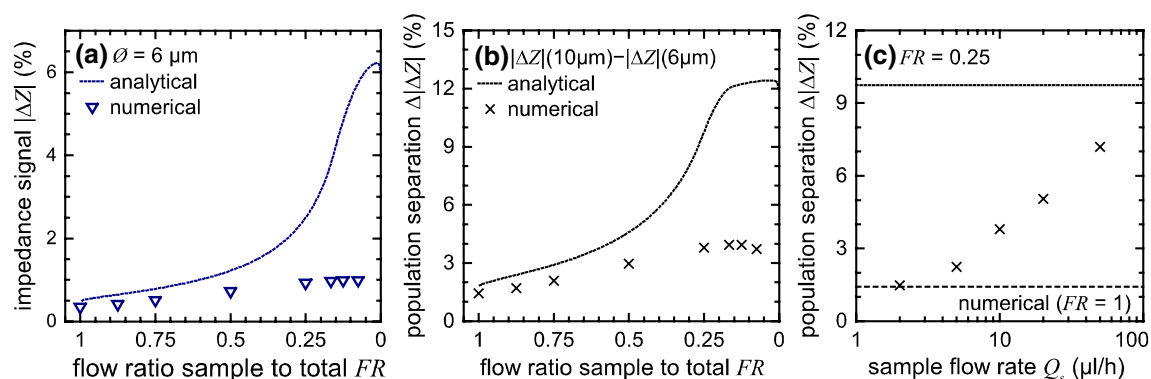

Fig. 4 Analytical (*dotted lines*) and numerical (*blue triangles, black crosses*) models of impedance cytometry performance as a function of (**a**, **b**) hydrodynamic focusing in terms of the flow ratio FR or of (**c**) sample flow rate Q_s at a representative, fixed FR = 0.25 (numeri-cal limit for FR = 1 indicated with *black dashed line*). Performance is shown in terms of (**a**) impedance cytometry signals $|\Delta Z|$ for cells of diameter $\varnothing = 6$ μm and of (**b**, **c**) population separation $\Delta|\Delta Z|$ between $\varnothing = 10$ and 6 μm diameter cells (color figure online)

(dotted line) for faster flow rates, which imply shorter diffusion times and, in turn, a more well-defined virtual aperture (VA). At low flow rates, the nearly complete interdiffusion between streams is equivalent to a simple change in conductivity σ_{el}, the cytometry performance thus approaching the limit of no flow focusing, *i.e.* FR = 1 (dashed line).

The trends here bear comparison with the hydrodynamic model ones in Fig. 3a, b. There, disagreement between models grows (in relative terms) gradually with flow ratio FR. This contrasts with the electrodynamic models, where model differences drastically increase below FR = 0.5. In the latter case, relative deviation moreover surpasses the approximately 20 % seen in hydrodynamic modeling by an order of magnitude. Conversely, hardly any deviation is apparent for the empty channel impedance Z_{empty} (not shown), where we find good overall agreement between analytical and numerical models at RMSE = 5.6 %. Z_{empty} is expected to be directly proportional to the conductive volume and thus to the virtual aperture width VA. In terms of the sample flow rate Q_s, the hydrodynamic models converge rapidly with increasing speeds, while the approach is very gradual in the electrodynamic ones. The experimental conditions fall close to the analytical limit in the former case, while not even clearing the half-way point between lower and upper limits for the latter one.

All of this establishes a rather curious implication: for an empty channel, the impact of ionic diffusion is even less than expected from hydrodynamic model considerations, while its impact significantly exceeds those expectations once a cell is introduced. The role of ionic diffusion thus appears much amplified where impedance cytometry is concerned, especially for low flow ratios FR < 0.5, compared to considering hydrodynamic focusing alone. From a modeling standpoint, these considerations imply that the formulation of Eq. 3 captures the virtual aperture width VA well with regard to the overall hydrodynamic focusing effect. However, the dominant factors with respect to impedance cytometry appear not suitably accounted for. Partial least squares (PLS) analysis indicates that the relative importance of the parameters scales as $C_{offset} > s_p \approx C_{amp} > s_s$ in terms of their impact on the numerically modeled $\Delta|\Delta Z|$. However, more work is required to fully explore the model interdependencies. We note that the impact of ionic diffusion in microfluidics appears to often be underappreciated, receiving attention in only few works on similar systems (Nasir et al. 2010; Golden et al. 2012). For our device, the typical measure of the relative importance of convection versus diffusion, the Péclet number, is $Pe = 4(Q_s + Q_f)/(2(w + h) \times D_{ion}) = 189$. Clearly much larger than 1, this would lead to the ab initio expectation of negligible diffusive effects, an assumption that is refuted throughout this work.

3.2 Part B: device experiments

In the theoretical discussions of Part A, we have observed interesting correlations between parameters, but also faced limitations for both analytical and numerical models. In Part B, we now seek to enhance our understanding of the phenomena at play employing the LOC platform shown in Fig. 1a. Utilizing the solely diameter-sensitive frequency of 100 kHz allows us to substitute polystyrene particles of similar diameters as red and white blood cells without compromising the general applicability of our work. As in Part A, we investigate the impact of the flow ratio FR, as well as the focus channel width w_{fc} as an exemplary geometric parameter on impedance cytometry performance. Moreover, we consider the unexpected, model-predicted large impact of ionic diffusion. Only through experimental data—and its comparison with the models—can we ensure that our insights on the interplay between in-plane hydrodynamic focusing and impedance cytometry are well founded.

3.2.1 Exemplary impedance data

We illustrate the operation of our LOC in Fig. 5a with representative impedance signal $|\Delta Z|$ measurements of ⌀ = 6 μm diameter particles over time for the lowest investigated flow ratio FR = 0.875. The processed data show a highly populated background at $|\Delta Z|$ = 0 %, as well as distinct points $|\Delta Z|$ > 0 % corresponding to particles passing between the electrodes, with clustering into a distinct band visually apparent. This is readily quantified through the subsequent transformation of the entire 30-min dataset into a histogram (Fig. 5b), where we determine the population average $|\Delta Z|$ = 0.16 % as well as the corresponding population spread δ = 0.02 % through Gaussian peak fitting between the first and second distribution minima, which serves as a reasonable first-order approximation. The signals observed inbetween the particle band and the background can be attributed to the instrumentation's transfer function adding a negative skew to the signal distribution, while those at $|\Delta Z|$ ~ 0.3 % are due to coincident detection of two particles, a phenomenon that cannot be entirely eliminated. As hydrodynamic focusing does not affect particle count results, these are not considered in our study.

It is the population average $|\Delta Z|$, the population spread δ, and the population separation $\Delta|\Delta Z|$ that determine the sensitivity of the LOC. To investigate the interplay of flow focusing and impedance cytometry, we collect at least 1000 particle signals at each of a range of flow ratios FR with each device and analyze the data accordingly. In Fig. 5c, we show population averages and spreads (symbols and error bars, respectively) from a representative device for
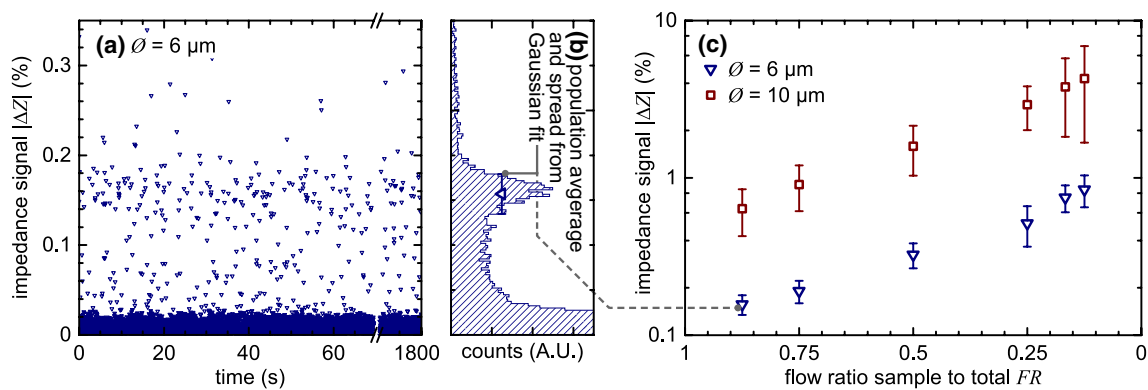
Fig. 5 a Representative processed experimental impedance cytometry signals $|\Delta Z|$ from $\varnothing = 6$ μm diameter particles at the lowest investigated FR = 0.875. **b** Corresponding histogram for the entire 30-min dataset, where population average $|\Delta Z|$ and spread δ (overlaid *blue triangle* and *error bar*, respectively) can be determined from Gauss-ian fitting between the first and second minima. **c** $|\Delta Z|$ and δ (*symbols* and *error bars*, respectively) for both $\varnothing = 6$ μm (*blue triangles*) and 10 μm (*red squares*) particle populations for a range of flow ratios FR from a representative device (color figure online)

both $\varnothing = 6$ and 10 μm particles, plotted with a logarithmic y-axis to present trends for both populations. The over five-fold increase in impedance signals $|\Delta Z|$ with increasing flow focusing (*i.e.*, decreasing FR) is readily apparent, as is the clear separation between populations, validating the general hypothesis. Since experiments using just a single LOC can suffer from outliers such as the large spreads δ seen here at low FR for the 10 μm population, we generally consider aggregate data across devices in our further analysis of impedance cytometry performance in Sects. 3.2.2 and 3.2.3.

3.2.2 Comparison of experiments and models

In Fig. 6a, we plot experimental population averages $|\Delta Z|$ as a function of flow ratio FR for $\varnothing = 6$ μm particles from each device (symbols). The corresponding analytical (dashed line) and numerical (dotted line) models are overlaid. We plot data along different y-axes (left—experiments; right—models), scaled by a factor of 3, to emphasize trends rather than absolute magnitudes. Looking first at the experimental data, we observe an over fivefold enhancement in
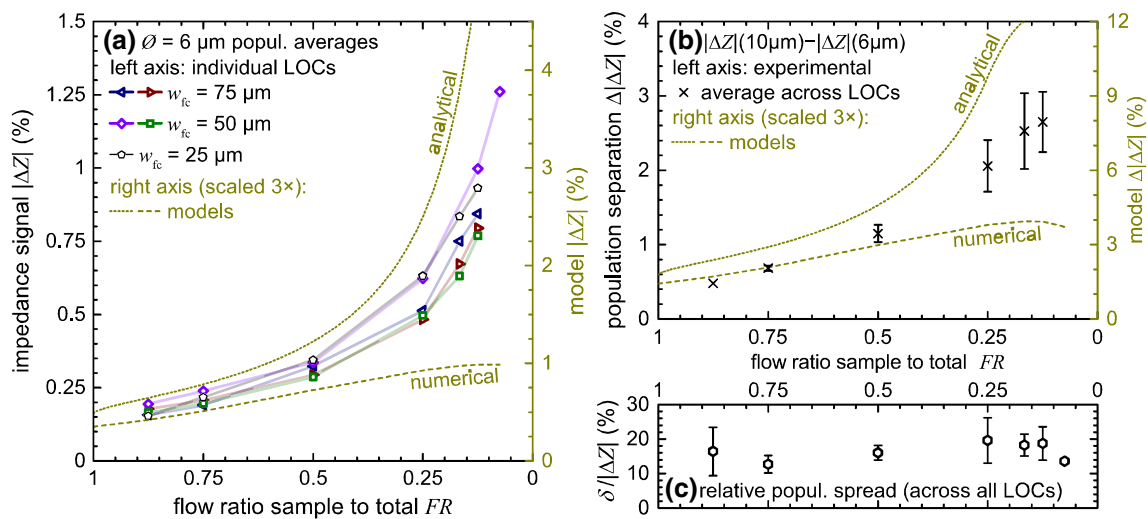

Fig. 6 a (*left axis*) Experimental impedance cytometry population averages $|\Delta Z|$ of $\varnothing = 6$ μm diameter particles (*symbols*) from all LOCs as a function of the flow ratio FR. Each *data point* here represents an average of at least 1000 particle passages. Connecting *solid lines* are visual guides only. (*right axis*) Corresponding analytical (*dotted*) and numerical (*dashed*) model predictions are overlaid, scaled by a factor of 3 to highlight trends. **b** Population separation $\Delta|\Delta Z|$ between $\varnothing = 6$ and 10 μm as an average across LOCs (*crosses*; *left axis*), with corresponding models overlaid scaled by a factor of 3 (*lines*; *right axis*). *Error bars* represent standard errors of the mean. **c** Average relative population spread $\delta/|\Delta Z|$ corresponding to the population averages in **a** across all devices (*hexagons*) shown separately for clarity. *Error bars* represent standard errors of the mean (color figure online)

$\varnothing = 6$ μm signals in all devices, from $|\Delta Z| = 0.17$–0.87 % at FR $= 0.125$ (averaged across devices).

The comparison between models and experiments proves interesting. The experimental $|\Delta Z|$ population averages lag behind predicted ones by a factor of approximately 3 (± 0.5, depending on the model) at high FR > 0.5, reflected in the different y-axes scales. However, they approach—and for some devices, surpass—the numerical model predictions at low FR. We attribute a large part of the generally lower signals to a transient averaging effect. The particle residence time within the interaction volume V, *i.e.* approximately $(Q_s + Q_f)/V$, is on a similar magnitude as the instrument sampling time $1/f_s$. Thus, the instrumentation circuitry captures an average $|\Delta Z|$ of the particle moving across the electrodes, rather than the modeled ideal $|\Delta Z|$ of a stationary particle suspended centrally between. Transient numerical studies, validated by experiments at low flow rates, indicate this transfer function effect accounts for a factor of ≈ 1.7. We attribute the remaining deviation to parasitic effects from the (compared to channel width w) long on-chip electrode traces and large connection pads, which the models ignore, as well as to likely underestimation of the medium conductivity (for low ionic concentration) and the ionic double layer capacitance from the employed approximations.

More important than the magnitudes, however, are the observed trends in $|\Delta Z|$. In this respect, we find that experiments actually follow the analytical model trend more closely than the numerical one in the low FR < 0.5 regime. This unexpected observation indicates that the latter does not fully describe the system; rather, it may provide a lower bound for predicted $|\Delta Z|$, once parasitic and transient effects are accounted for. The analytical model, conversely, yields an upper bound. We hypothesize that neglected higher-order hydrodynamic effects yield an experimental trend that falls between the extremes of the two modeling approaches.

In Fig. 6b, we plot the separation between the $\varnothing = 6$ and 10 μm diameter particle populations $\Delta |\Delta Z|$ as a function of flow ratio FR. Experimental data (averaged across devices; crosses) are overlaid by corresponding analytical (dashed line) and numerical (dotted line) models. As previously, the y-axes are distinct for experimental (left) and model (right) data, with a scaling factor of 3. The population separation performance metric exhibits a similar trend to $|\Delta Z|$, with an over fivefold increase from $\Delta |\Delta Z| = 0.48$–2.65 % toward the lowest FR. The comparison with model data follows nearly identical patterns to those in Fig. 6a for $|\Delta Z|$. These observations validate the conclusions drawn above, as $\Delta |\Delta Z|$ additionally incorporates the independent $\varnothing = 10$ μm data in the analysis. Importantly, these results serve to highlight the real advantages in terms of sensitivity of integrating impedance cytometry with in-plane hydrodynamic focusing.

3.2.3 Impedance signal spread

Population spreads δ corresponding to the population averages in Fig. 6a are displayed separately in Fig. 6c, in terms of relative $\delta/|\Delta Z|$ averaged across devices. The trend proves practically constant with a mean $\delta/|\Delta Z| = 16$ % across all FR. The visual observation is statistically backed up by linear regression model ANOVA yielding a p value of $p = 0.15$, *i.e.* an insignificant trend. This indicates that the observed population spreads are dominated by two factors. First, there is inherent variation in particle diameters around their nominal specifications, specifically 22 % in terms of volume (which is proportional to the measured impedance changes). Second, the stochastic positioning of particles in the vertical z dimension results in unavoidable signal variations due to the non-homogenous electric field, more pronounced for our case of co-planar electrodes. For this type of geometry, Gawad et al. (2001) predict on the order of 30 % spread for $\varnothing = 10$ μm particles. Compared to both this prediction and the intrinsic particle volume variation, our figures are not unfavorable. Both of the aforementioned factors are proportionally amplified by enhanced sensitivity and thus match our observed constant $\delta/|\Delta Z|$. If the third likely candidate for noise in the system—syringe pump stepping causing fluctuations in FR—were dominant, an increasing trend with decreasing FR would be expected, being independent of $|\Delta Z|$. We note that although the signal spreads are relatively large, they do not infringe upon our broader conclusions, which are otherwise based on the population means and their standard errors of less than 5 %.

3.2.4 Impact of geometry and ionic diffusion

Looking again at the impedance signals $|\Delta Z|$ for the various devices in Fig. 6a, although the trends are similar, we nevertheless observe discrepancies between LOCs of RMSE $= 9.5$ % (relative to the respective average $|\Delta Z|$, across all FR). This may point toward the impact of geometrical variations between those devices. The main geometrical design parameter to be investigated in this study with respect to its impact on in-plane hydrodynamic focusing and impedance cytometry is the focus channel width w_{fc}. Thus, we consider the $|\Delta Z|$ data presented in Fig. 6a as a function of w_{fc} at each flow ratio FR. While modeling did not predict a significant impact of this parameter on $|\Delta Z|$, it is, nevertheless, the prime candidate to explain the cross-device variability seen in Fig. 6a. However, the correlation of impedance signals $|\Delta Z|$ with focus channel width w_{fc} proves insignificant. Linear regression model ANOVA yields an average p value (across all FR) of $\bar{p}(w_{fc}) = 0.40$. This experimentally verifies the model prediction that w_{fc} does not significantly impact hydrodynamic focusing or impedance cytometry.
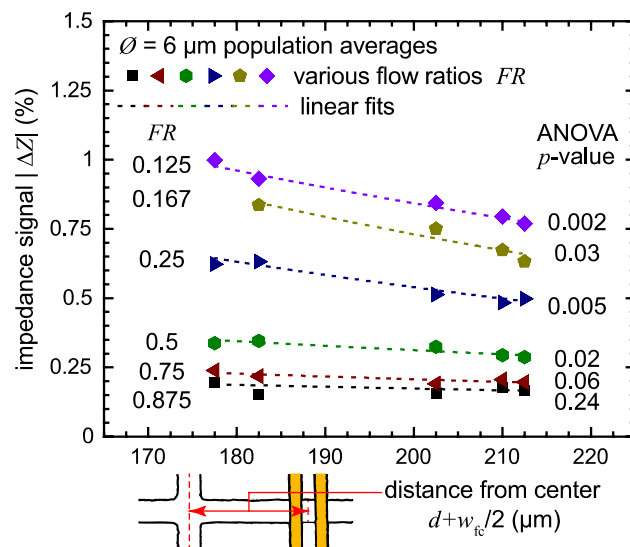
Fig. 7 Experimental impedance cytometry population averages $|\Delta Z|$ of ⌀ = 6 μm diameter particles recorded using different LOCs as a function of the distance $d' = d + w_{fc}/2$. The geometrical parameter is highlighted in the *schematic drawing* of the device layout. FR is listed on the *left* for each set of data and decreases from 0.875 (*black squares*) to 0.125 (*purple diamonds*). Linear fits to the data are shown as *dotted lines*, and p values of corresponding ANOVA models are listed on the *right* (color figure online)

Since models did predict a significant impact of diffusion, we consider related device parameters to explain the cross-LOC variations from Fig. 6a. In particular, the distance d from the downstream edge of the focusing junction to the center of the electrodes is expected to be proportional to ionic diffusion effects. A longer d equals more time for diffusion of ions from the sample flow into the pure water sheath flows prior to measurement, weakening the virtual aperture (VA). Thus, we utilize the fabrication verification data for each device to consider the impact of variations in d from manual alignment of the top and bottom layers (as per the specifications within 10 % of $d = 170$ μm). Still, we do not observe a dependence of device performance in $|\Delta Z|$ with d itself. Curiously, when we consider instead the distance $d' = d + w_{fc}/2$, *i.e.* measured from the center of the focusing junction to the center of the electrodes, we observe a strong negative correlation with $|\Delta Z|$, especially at low flow ratios FR. This is illustrated in Fig. 7, where experimental impedance signals $|\Delta Z|$ are plotted as a function of d'. Conversely—like d itself—the third intuitive option for expressing the downstream distance as $d'' = d + w_{fc}$ fails to show an appreciable trend. Linear regression model ANOVA supports our analysis, with $\bar{p}(d) = 0.22$, $\bar{p}(d'') = 0.06$, and $\bar{p}(d'') = 0.13$. While slightly above the traditional significance level, d' represents the only parameter with consistent $p < 0.05$ for each flow ratio FR < 0.75, where any geometrical effects on diffusion

would be expected to be more pronounced due to the narrower virtual aperture (VA). Although a linear regression model may not fully capture the correlation of d' and $|\Delta Z|$, we posit that it is a sufficient approximation over the range of parameters investigated. We note that the impact of variations in channel height h due to photoresist spinning, which could also be expected to impact sensitivity through altering the interaction volume V, is insignificant at $\bar{p}(h) = 0.93$.

Overall, this result experimentally validates the theoretically predicted importance of diffusion even at high Péclet number with regard to impedance cytometry. The previously unobserved correlation of performance with the center-to-center distance d' aligns with other research on geometrical effects, where inertial flow effects were shown play a large role in hydrodynamic focusing (Nasir et al. 2011; Kunstmann-Olsen et al. 2012). Such inertial effects would be expected to correlate strongly with the channel centers, where the linear flow speeds are highest. For impedance cytometry sensitivity, this implies that, indirectly, focus channel width w_{fc} has an impact after all and that minimal d'—i.e., both a short d as well as a narrow w_{fc}—is required for optimization.

4 Conclusions

In conclusion, our in-depth study of systems integration showcases the interplay of impedance cytometry and in-plane hydrodynamic focusing. Compared to physical channel constriction, this approach offers a distinctly lower risk of clogging and provides tunable, rather than static, sensitivity and throughput. We explore it from both theoretical and experimental perspectives, developing novel modeling approaches, and providing a simple yet efficient platform with our device. We demonstrate an over fivefold enhancement in impedance signals as well as in population separation. We find that ionic diffusion must not be neglected for such systems even at high Péclet number. This is in line with previous work preferring immiscible two-phase flows of oil and water, albeit without much underlying discussion (Bernabini et al. 2011; Evander et al. 2013), a scenario where our analytical model should prove highly descriptive. Still, we posit that our approach in utilizing pure water is preferable for point-of-care applications. The aforementioned immiscible two-phase flows can suffer from interfacial instabilities, making hydrodynamic control more challenging (Nieuwenhuis et al. 2004; Golden et al. 2012). Moreover, pure water reduces the reagent requirements of the device; DI or distilled water is cheap, readily available, and even in very resource-poor settings could be produced on location. Here, analytical and numerical model trends serve as upper and lower bounds for the experimentally

observed one. Our study of geometry variations in hydrodynamic focusing reveals limited direct impact on impedance cytometry. However, we show that the distance of cytometry electrodes from the focusing junction center, rather than its downstream edge, strongly correlates with performance. Indirectly impacted by the channel geometry, this phenomenon can be related to inertial flow effects and furthermore highlights the importance of ionic diffusion.

Our design allows for straightforward expansion to multi-frequency signal recording, and our in-plane study provides a foundation for a range of out-of-plane focusing approaches. This will ultimately provide high-resolution multi-dimensional particle characterization toward an integrated microsystem capable of full differential blood cell counting. Furthermore, our approach illustrates the benefits of model-guided design as well as in-depth examination of systems interplay in LOC devices. With many examples of exciting LOC technologies—sensors, blood-handling components, microfluidic components—published in the literature, we believe it is only through such studies that they can be optimally realized in integrated point-of-care microsystems.

References

Analog Devices (2005) AD5933 Impedance converter network analyzer. http://www.analog.com/en/products/rf-microwave/direct-digital-synthesis-modulators/ad5933.html

Asami K, Hanai T, Koizumi N (1980) Dielectric approach to suspensions of ellipsoidal particles covered with a shell in particular reference to biological cells. Jpn J Appl Phys 19:359–365. doi:10.1143/JJAP.19.359

Ateya DA, Erickson JS, Howell PB Jr et al (2008) The good, the bad, and the tiny: a review of microflow cytometry. Anal Bioanal Chem 391:1485–1498. doi:10.1007/s00216-007-1827-5

Bashir R (2004) BioMEMS: state-of-the-art in detection, opportunities and prospects. Adv Drug Deliv Rev 56:1565–1586. doi:10.1016/j.addr.2004.03.002

Ben-Yoav H, Dykstra PH, Gordonov T et al (2014) A microfluidic-based electrochemical biochip for label-free DNA hybridization analysis. J Vis Exp. doi:10.3791/51797

Berg HC (1993) Random walks in biology. Princeton University Press, Princeton

Bernabini C, Holmes D, Morgan H (2011) Micro-impedance cytometry for detection and analysis of micron-sized particles and bacteria. Lab Chip 11:407–412. doi:10.1039/c0lc00099j

Chen J, Xue C, Zhao Y et al (2015) Microfluidic impedance flow cytometry enabling high-throughput single-cell electrical property characterization. Int J Mol Sci 16:9804–9830. doi:10.3390/ijms16059804

Cheung K, Gawad S, Renaud P (2005) Impedance spectroscopy flow cytometry: on-chip label-free cell differentiation. Cytom A 65A:124–132. doi:10.1002/cyto.a.20141

Cheung KC, Di Berardino M, Schade-Kampmann G et al (2010) Microfluidic impedance-based flow cytometry. Cytometry A 77A:648–666. doi:10.1002/cyto.a.20910

DeBlois RW, Bean CP (1970) Counting and sizing of submicron particles by the resistive pulse technique. Rev Sci Instrum 41:909–916. doi:10.1063/1.1684724

Evander M, Ricco AJ, Morser J et al (2013) Microfluidic impedance cytometer for platelet analysis. Lab Chip 13:722–729. doi:10.1039/c2lc40896a

Frankowski M, Simon P, Bock N et al (2015) Simultaneous optical and impedance analysis of single cells: a comparison of two microfluidic sensors with sheath flow focusing. Eng Life Sci 15:286–296. doi:10.1002/elsc.201400078

Gawad S, Schild L, Renaud P (2001) Micromachined impedance spectroscopy flow cytometer for cell analysis and particle sizing. Lab Chip 1:76–82. doi:10.1039/b103933b

Gawad S, Cheung K, Seger U et al (2004) Dielectric spectroscopy in a micromachined flow cytometer: theoretical and practical considerations. Lab Chip 4:241–251. doi:10.1039/b313761a

Golden JP, Justin GA, Nasir M, Ligler FS (2012) Hydrodynamic focusing—a versatile tool. Anal Bioanal Chem 402:325–335. doi:10.1007/s00216-011-5415-3

Han X, van Berkel C, Gwyer J et al (2012) Microfluidic lysis of human blood for leukocyte analysis using single cell impedance cytometry. Anal Chem 84:1070–1075. doi:10.1021/ac202700x

Holmes D, Pettigrew D, Reccius CH et al (2009) Leukocyte analysis and differentiation using high speed microfluidic single cell impedance cytometry. Lab Chip 9:2881–2889. doi:10.1039/b910053a

Johnson AM, Sadoway DR, Cima MJ, Langer R (2005) Design and testing of an impedance-based sensor for monitoring drug delivery. J Electrochem Soc 152:H6–H11. doi:10.1149/1.1824045

Jung W, Han J, Choi J-W, Ahn CH (2015) Point-of-care testing (POCT) diagnostic systems using microfluidic lab-on-a-chip technologies. Microelectron Eng 132:46–57. doi:10.1016/j.mee.2014.09.024

Kottke-Marchant K, Davis B (2012) Laboratory hematology practice. Wiley, Chichester

Kunstmann-Olsen C, Hoyland JD, Rubahn H-G (2012) Influence of geometry on hydrodynamic focusing and long-range fluid behavior in PDMS microfluidic chips. Microfluid Nanofluid 12:795–803. doi:10.1007/s10404-011-0923-1

Lee G-B, Chang C-C, Huang S-B, Yang R-J (2006) The hydrodynamic focusing effect inside rectangular microchannels. J Micromech Microeng 16:1024–1032. doi:10.1088/0960-1317/16/5/020

Lide DR, Kehiaian HV (1994) CRC handbook of thermophysical and thermochemical data. CRC Press, Boca Raton

Mansor MA, Ahmad MR (2015) Single cell electrical characterization techniques. Int J Mol Sci 16:12686–12712. doi:10.3390/ijms160612686

Meyer MT, Subramanian S, Kim YW et al (2015) Multi-depth valved microfluidics for biofilm segmentation. J Micromech Microeng 25:95003. doi:10.1088/0960-1317/25/9/095003

Morgan H, Sun T, Holmes D et al (2007) Single cell dielectric spectroscopy. J Phys Appl Phys 40:61–70. doi:10.1088/0022-3727/40/1/S10

Nasir M, Price DT, Shriver-Lake LC, Ligler F (2010) Effect of diffusion on impedance measurements in a hydrodynamic flow focusing sensor. Lab Chip 10:2787–2795. doi:10.1039/C005257D

Nasir M, Mott DR, Kennedy MJ et al (2011) Parameters affecting the shape of a hydrodynamically focused stream. Microfluid Nanofluid 11:119–128. doi:10.1007/s10404-011-0778-5

Nguyen J, Wei Y, Zheng Y et al (2015) On-chip sample preparation for complete blood count from raw blood. Lab Chip 15:1533–1544. doi:10.1039/C4LC01251H

Nieuwenhuis JH, Kohl F, Bastemeijer J et al (2004) Integrated Coulter counter based on 2-dimensional liquid aperture control. Sens Actuat B Chem 102:44–50. doi:10.1016/j.snb.2003.10.017

Pitts E, Tabor BE (1970) Concentration dependence of electrolyte conductance. Part 2—comparison of experimental data with the Fuoss-Onsager and Pitts treatments. Trans Faraday Soc 66:693–707. doi:10.1039/TF9706600693

Rodriguez-Trujillo R, Mills CA, Samitier J, Gomila G (2007) Low cost micro-Coulter counter with hydrodynamic focusing. Microfluid Nanofluid 3:171–176. doi:10.1007/s10404-006-0113-8

Rodriguez-Trujillo R, Castillo-Fernandez O, Garrido M et al (2008) High-speed particle detection in a micro-Coulter counter with two-dimensional adjustable aperture. Biosens Bioelectron 24:290–296. doi:10.1016/j.bios.2008.04.005

Shapiro HM (2003) Practical flow cytometry. Wiley, Hoboken

Siggaard-Andersen O, Durst RA, Maas AHJ (1984) Physicochemical quantities and units in clinical chemistry with special emphasis on activities and activity coefficients (Recommendations 1983). Pure Appl Chem 56:567–594. doi:10.1351/pac198456050567

Sun T, Morgan H (2010) Single-cell microfluidic impedance cytometry: a review. Microfluid Nanofluid 8:423–443. doi:10.1007/s10404-010-0580-9

Sun T, Gawad S, Green NG, Morgan H (2007a) Dielectric spectroscopy of single cells: time domain analysis using Maxwell's mixture equation. J Phys Appl Phys 40:1–8. doi:10.1088/0022-3727/40/1/S01

Sun T, Green NG, Gawad S, Morgan H (2007b) Analytical electric field and sensitivity analysis for two microfluidic impedance cytometer designs. IET Nanobiotechnol 1:69–79. doi:10.1049/iet-nbt:20070019

Sun T, Green NG, Morgan H (2008) Analytical and numerical modeling methods for impedance analysis of single cells on-chip. Nano 3:55–63. doi:10.1142/S1793292008000800

Sun T, Bernabini C, Morgan H (2010) Single-colloidal particle impedance spectroscopy: complete equivalent circuit analysis of polyelectrolyte microcapsules. Langmuir 26:3821–3828. doi:10.1021/la903609u

van Berkel C, Gwyer JD, Deane S et al (2011) Integrated systems for rapid point of care (PoC) blood cell analysis. Lab Chip 11:1249–1255. doi:10.1039/C0LC00587H

Watkins N, Venkatesan BM, Toner M et al (2009) A robust electrical microcytometer with 3-dimensional hydrofocusing. Lab Chip 9:3177–3184. doi:10.1039/B912214A

Xuan X, Zhu J, Church C (2010) Particle focusing in microfluidic devices. Microfluid Nanofluid 9:1–16. doi:10.1007/s10404-010-0602-7